



AnaXNet: Anatomy Aware Multi-label Finding Classification in Chest X-Ray

Nkechinyere N. Agu¹(✉), Joy T. Wu², Hanqing Chao¹, Ismini Lourentzou³,
Arjun Sharma², Mehdi Moradi², Pingkun Yan¹, and James Hendler¹

¹ Rensselaer Polytechnic Institute, Troy, NY 12180, USA
agun@rpi.edu

² IBM Research, Almaden Research Center, San Jose, CA 95120, USA

³ Virginia Tech, Blacksburg, VA 24061, USA

Abstract. Radiologists usually observe anatomical regions of chest X-ray images as well as the overall image before making a decision. However, most existing deep learning models only look at the entire X-ray image for classification, failing to utilize important anatomical information. In this paper, we propose a novel multi-label chest X-ray classification model that accurately classifies the image finding and also localizes the findings to their correct anatomical regions. Specifically, our model consists of two modules, the detection module and the anatomical dependency module. The latter utilizes graph convolutional networks, which enable our model to learn not only the label dependency but also the relationship between the anatomical regions in the chest X-ray. We further utilize a method to efficiently create an adjacency matrix for the anatomical regions using the correlation of the label across the different regions. Detailed experiments and analysis of our results show the effectiveness of our method when compared to the current state-of-the-art multi-label chest X-ray image classification methods while also providing accurate location information.

Keywords: Graph convolutional networks · Multi-label chest X-ray image classification · Graph representation

1 Introduction

Interpreting a radiology imaging exam is a complex reasoning task, where radiologists are able to integrate patient history and image features from different anatomical locations to generate the most likely diagnoses. Convolutional Neural Networks (CNNs) have been widely applied in earlier works in automatic Chest X-ray (CXR) interpretation, one of the most commonly requested medical imaging modality. Many of these works have framed the problem either as a multi-label abnormality classification problem [18, 27], an abnormality detection and localization problem [5, 22, 29], or an image-to-text report generation problem [14, 28]. However, these models fail to capture inter-dependencies between

features or labels. Leveraging such contextual information that encodes relational information among pathologies is crucial in improving interpretability and reasoning in clinical diagnosis.

To this end, Graph Neural Networks (GNN) have surfaced as a viable solution in modeling disease co-occurrence across images. Graph Neural Networks (GNNs) learn representations of the nodes based on the graph structure and have been widely explored, from graph embedding methods [7, 23], generative models [25, 32] to attention-based or recurrent models [15, 24], among others. For a comprehensive review on model architectures, we refer the reader to a recent survey [31]. In particular, Graph Convolutional Networks (GCNs) [13] utilize *graph convolution* operations to learn representations by aggregating information from the neighborhood of a node, and have been successfully applied to CXR image classification. For example, the multi-relational ImageGCN model learns image representations that leverage additional information from related images [17], while CheXGCN and DD-GCN incorporate label co-occurrence GCN modules to capture the correlations between labels [2, 16]. To mitigate the issues with noise originating from background regions in related images, recent work utilizes attention mechanisms [1, 34] or auxiliary tasks such as lung segmentation [3, 6]. However, none of these works consider modeling correlations among anatomical regions and findings, *e.g.*, output the anatomical location semantics for each finding.

We propose a novel model that captures the dependencies between the anatomical regions of a chest X-ray for classification of the pathological findings, termed **Anatomy-aware X-ray Network** (AnaXNet). We first extract the features of the anatomical regions using an object detection model. We develop a method to accurately capture the correlations between the various anatomical regions and learn their dependencies with a GCN model. Finally, we combine the localized region features via attention weights computed with a non-local operation [26] that resembles self-attention.

The main contributions of this paper are summarized as follows: 1) we propose a novel multi-label CXR findings classification framework that integrates both global and local anatomical visual features and outputs accurate localization of clinically relevant anatomical regional levels for CXR findings, 2) we propose a method to automatically learn the correlation between the findings and the anatomical regions and 3) we conduct in-depth experimental analysis to demonstrate that our proposed AnaXNet model outperforms previous baselines and state-of-the-art models.

2 Methodology

We first describe our proposed framework for multi-label chest X-ray classification. Let CXR image collection comprised of a set of N chest-X ray images $\mathcal{C} = \{x_1, \dots, x_N\}$, where each image x_i is associated with a set of M labels $\mathcal{Y}_i = \{y_i^1, \dots, y_i^M\}$, with $y_i^m \in \{0, 1\}$ indicating whether the label for pathology M appears in image x_i or not. Then the goal is to design a model that predicts the label set for an unseen image as accurately as possible, by utilizing

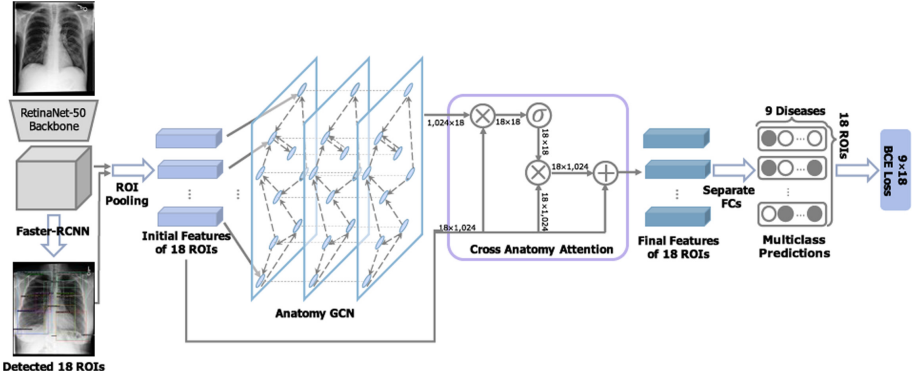


Fig. 1. Model overview. We extract anatomical regions of interest (ROIs) and their corresponding features, feed their vectors to a Graph Convolutional Network that learns their inter-dependencies, and combine the output with an attention mechanism, to perform the final classification with a dense layer. Note that throughout the paper, we use the term *bounding box* instead of ROI.

the correlation among anatomical region features $R_i = f(x_i) \in \mathbb{R}^{k \times d}$, where k is the number of anatomical region embedding, each with dimensionality d . The anatomical region feature extractor f is described in Subsect. 3.3.

Given this initial set of anatomical region representations R_i , we define a normalized adjacency matrix $A \in \mathbb{R}^{k \times k}$ that captures region correlations, and utilize a GCN $Z_i = g(R_i, A) \in \mathbb{R}^{k \times d}$ to update R_i as follows:

$$R_i^{t+1} = \phi(AR_i^t W_1^t), \quad (1)$$

where $W_1^t \in \mathbb{R}^{d \times d}$ is the learned weight matrix and $\phi(\cdot)$ denotes a non-linear operation, *e.g.*, ReLU [33] in our experiments, and t is the number of stacked GCN layers. To construct the adjacency matrix A , we extract co-occurrence patterns between anatomical regions for label pairs. More specifically, the label co-occurrence matrix can be computed based on Jaccard similarity:

$$J(r_i, r_j) = \frac{1}{M} \sum_{m=1}^M \frac{|\mathcal{Y}_i^m \cap \mathcal{Y}_j^m|}{|\mathcal{Y}_i^m \cup \mathcal{Y}_j^m|}, \quad (2)$$

where r_i and r_j represent anatomical regions, \mathcal{Y}_i is the set for region r_i and label m across all images and \cap, \cup denote the intersection and union over multi-sets. However, this label co-occurrence construction may overfit the training data due to incorporating noisy rare occurrences. To mitigate such issues, we use a filtering threshold τ , *i.e.*,

$$A_{ij} = \begin{cases} 1 & \text{if } J(R_i, R_j) \geq \tau \\ 0 & \text{if } J(R_i, R_j) < \tau \end{cases}, \quad (3)$$

where A is the final adjacency matrix.

Table 1. Dataset characteristics. # Images (number of images) and # Bboxes (number of bounding boxes) labeled with L1-L9. There are a total of 217,417 images in the dataset, of which 153,333 have at least one of the L1-L9 labels globally. Of these images, 3,877,010 bounding boxes were extracted automatically and 720,098 of them have at least one or more of the 9 labels.

Label ID	Description	# Images (1)	# Bboxes
L1	Lung opacity	132,981	584,638
L2	Pleural effusion	68,363	244,005
L3	Atelectasis	76,868	240,074
L4	Enlarged cardiac silhouette	55,187	58,929
L5	Pulmonary edema/hazy opacity	33,441	145,965
L6	Pneumothorax	9,341	22,906
L7	Consolidation	16,855	53,364
L8	Fluid overload/heart failure	6,317	18,066
L9	Pneumonia	32,042	95,215
All 9 labels	Positive/total	153,333/217,417	720,098/3,877,010

To capture both global and local dependencies between anatomical regions, we leverage a non-local operation that resembles self-attention [26]:

$$Q_i = \text{softmax}(R_i Z_i^T) R_i, \quad (4)$$

where $Q_i \in \mathbb{R}^{k \times d}$. The final prediction is computed via

$$\hat{y} = [R_i; Q_i] W_2^T, \quad (5)$$

where $W_2 \in \mathbb{R}^{2d \times M}$ is a fully connected layer to obtain the label predictions. The network is trained with a multi-label cross-entropy classification loss

$$L = \frac{1}{N} \sum_{i=1}^N \sum_{m=1}^M y_i^m \log(\sigma(\hat{y}_i^m)) + (1 - y_i^m) \log(1 - \sigma(\hat{y}_i^m)), \quad (6)$$

where σ is the Sigmoid function and $\{\hat{y}_i^m, y_i^m\} \in \mathbb{R}^M$ are the model prediction and ground truth for example x_i , respectively. The model architecture is summarized in Fig. 1.

3 Experiments

We describe experimental details, *i.e.*, evaluation dataset, metrics, *etc.*, and present quantitative and qualitative results, comparing AnaXNet with several baselines.

Table 2. Intersection over Union scores (IoU) are calculated between the automatically extracted anatomical bounding box (Bbox) regions and a set of single manual ground truth bounding boxes for 1000 CXR images. Average precision and recall across 9 CXR pathologies are shown for the NLP derived labels at: right lung (RL), right apical zone (RAZ), right upper lung zone (RULZ), right mid lung zone (RMLZ), right lower lung zone (RLLZ), right costophrenic angle (RCA), left lung (LL), left apical zone (LAZ), left upper lung zone (LULZ), left mid lung zone (LMLZ), left lower lung zone (LLLZ), left costophrenic angle (LCA), mediastinum (Med), upper mediastinum (UMed), cardiac silhouette (CS) and trachea (Trach).

Bbox abbreviation	RL	RAZ	RULZ	RMLZ	RLLZ	RHS	RCA	LL	LAZ
Bbox IoU	0.994	0.995	0.995	0.989	0.984	0.989	0.974	0.989	0.995
NLP precision	0.944	0.762	0.857	0.841	0.942	0.897	0.871	0.943	0.800
NLP recall	0.98	0.889	0.857	0.746	0.873	0.955	0.808	0.982	1.00
Bbox abbreviation	LULZ	LMLZ	LLLZ	LHS	LCA	Med	UMed	CS	Trach
Bbox IoU	0.995	0.986	0.979	0.985	0.950	0.972	0.993	0.967	0.983
NLP precision	0.714	0.921	0.936	0.888	0.899	N/A	N/A	0.969	N/A
NLP recall	0.938	0.972	0.928	0.830	0.776	N/A	N/A	0.933	N/A

3.1 Dataset

Existing annotations of large-scale CXR datasets [11,12,27] are either weak global labels for 14 common CXR findings extracted from reports with Natural Language Processing (NLP) methods [11], or are manually annotated with bounding boxes for a smaller subset of images and for a limited number of labels [4,21]. None of these annotated datasets describe the anatomical location for different CXR pathologies. However, localizing pathologies to anatomy is a key aspect of radiologists’ reasoning and reporting process, where knowledge of correlation between image findings and anatomy can help narrow down potential diagnoses.

The Chest ImaGenome dataset builds on the works of [29,30] to fill this gap by using a combination of rule-based text-analysis and atlas-based bounding box extraction techniques to structure the anatomies and the related pathologies from 217,417 report texts and frontal images (AP or PA view) from the MIMIC-CXR dataset [12]. In summary, the text pipeline [30] first sections the report and retains only the finding and impression sentences. Then it uses a prior curated CXR concept dictionary (lexicons) to identify and detect the context (negated or not) for name entities required for labeling the 18 anatomical regions and 9 CXR pathology labels from each retained sentence. The pathology labels are associated with the anatomical region described in the same sentence with a natural language parser, SpaCy [9], and clinical heuristics provided by a radiologist was used to correct for obvious pathology-to-anatomy assignment errors (e.g. lung opacity wrongly assigned to mediastinum). Finally the pathology label(s) for each of the 18 anatomical regions from repeated sentences are grouped to the exam level. A separate anatomy atlas-based bounding box pipeline extracts the coordinates from each frontal images for the 18 anatomical regions [29].

Table 3. Comparison of our approach against baselines (AUC score).

Method	L1	L2	L3	L4	L5	L6	L7	L8	L9	AVG
Faster R-CNN	0.84	0.89	0.77	0.85	0.87	0.77	0.75	0.81	0.71	0.80
GlobalView	0.91	0.94	0.86	0.92	0.92	0.93	0.86	0.87	0.84	0.89
CheXGCN	0.86	0.90	0.91	0.94	0.95	0.75	0.89	0.98	0.88	0.90
AnaXNet (ours)	0.88	0.96	0.92	0.99	0.95	0.80	0.89	0.98	0.97	0.93

Table 1 shows high-level statistics of the generated dataset. Dual annotations for 500 random reports (disagreement resolved via consensus) were curated at sentence level by a clinician and a radiologist, who also annotated the bounding boxes for 1000 frontal CXRs (single annotation). For the 9 pathology, the overall NLP average precision and recall without considering localization are 0.9819 and 0.9875, respectively. More detailed results by anatomical regions are shown in Table 2.

3.2 Baselines

The anatomical region feature extractor $f(x_i) \in \mathbb{R}^{k \times d}$ is a Faster R-CNN with with ResNet-50 [8] as base model. Additional implementation details, *e.g.*, hyper-parameters, are provided later on (Subsect. 3.3). We perform comprehensive analysis on the Chest ImaGenome dataset. We compare our AnaXNet model against: 1) **GlobalView** we implement a DenseNet169 [10] model as a baseline method to contrast the effectiveness of location-aware AnaXNet versus a global view of the image, 2) **Faster R-CNN** [19] followed by a fully-connected layer, *i.e.*, without the GCN and attention modules, to establish a baseline accuracy for the classification task using the extracted anatomical features, and 3) **CheXGCN** We re-implement the state-of-the-art model CheXGCN [2] that utilizes GCNs to learn the label dependencies between pathologies in the X-ray images. The model uses a CNN for feature extraction and a GCN to learn the relationship between the labels via word embeddings. We replace the overall CNN with Faster R-CNN for a fair comparison with our model, but retain their label co-occurrence learning module.

3.3 Implementation Details

We train the detection model to detect the 18 anatomical regions. To obtain the anatomical features, we take the final output of the model and perform non-maximum suppression for each object class using an IoU threshold. We select all the regions where any class probability exceeds our confidence threshold. We use a value of 0.5 for τ . For each region, we extract a 1024 dimension convolutional feature vector. For multiple predictions of the same anatomical region, we select the prediction with the highest confidence score and drop the duplicates. When the model fails to detect a bounding box, we use a vector of zeros to represent

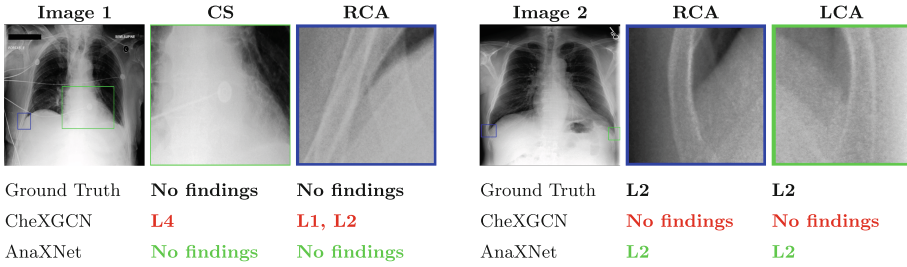


Fig. 2. Examples of the results obtained by our best two models. The overall chest X-ray image is shown alongside two anatomical regions. The predictions from best performing models are compared against the ground-truth labels.

the anatomical features of the region within the GCN. We use detectron2¹ to train Faster R-CNN to extract anatomical regions and their features. Our GCN model is made up of two GCN layers with output dimensionality of 512 and 1024 respectively. We train with Adam optimizer, and 10^{-4} learning rate for 25 epochs in total.

3.4 Results and Evaluation

Results are summarized in Table 3. The evaluation metric is Area Under the Curve (AUC). Note that the baseline GlobalView is in fact a global classifier and does not produce a localized label. The remaining rows in Table 3 show localized label accuracy. For the localized methods, the reported numbers represent the average AUC of the model for each label over the various anatomical regions. If a finding is detected at the wrong anatomical location, it counts as false detection. For fair comparison, we use the same 70/10/20 train/validation/testing split across patients to train each model. AnaXNet model obtains improvements over the previous methods while also localizing the diseases in their correct anatomical region. The GlobalView is most likely limited because it focuses on the entire image instead of a specific region.

The CheXGCN model outperforms the other two baselines but is also limited because it focuses on one section and uses label dependencies to learn the relationship between the labels, while ignoring the relationships between the anatomical regions of the chest X-ray image. In Table 2, we visualize the output from both the CheXGCN model and our AnaXNet model. The CheXGCN model had difficulty predicting small anatomical regions like the costophrenic angles, while our model had additional information from the remaining anatomical regions, which helped in its prediction. Also the CheXGCN model struggled with enlarged cardiac silhouette label because information from the surrounding labels is needed in order to accurately tell if the heart is enlarged.

In Fig. 3 we also visualize the output of Grad-CAM [20] method on the GlobalView model to highlight the importance of the localization, while the prediction

¹ <https://github.com/facebookresearch/detectron2>.

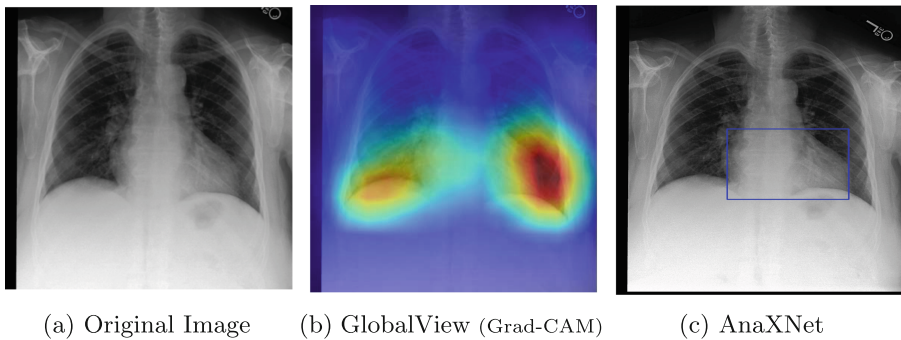


Fig. 3. An example image from our dataset with enlarged cardiac silhouette. The GlobalView network detects this label correctly, but as the Grad-CAM activation map shows (b), the attention of the network is not on the cardiac region. Our method detects the finding in the correct bounding box (c).

of Enlarged Cardiac Silhouette was correct, the GlobalView model was focused on the lungs. Our method was able to provide accurate localization information as well as the finding.

4 Conclusion

We described a methodology for localized detection of diseases in chest X-ray images. Both the algorithmic framework of this work, and the dataset of images labeled for pathologies in the semantically labeled bounding boxes are important contributions. For our AnaXNet design, a Faster R-CNN architecture detects the bounding boxes and embeds them. The resulting embedded vectors are then used as input to a GCN and an attention block that learn representations by aggregating information from the neighboring regions.

This approach accurately detects any of the nine studied abnormalities and places it in the correct bounding box in the image. The 18 pre-specified bounding boxes are devised to map to the anatomical areas often described by radiologists in chest X-ray reports. As a result, our method provides all the necessary components for composing a structured report. Our vision is that the output of our trained model, subject to expansion of the number and variety of findings, will provide both the finding and the anatomical location information for both downstream report generation and other reasoning tasks. Despite the difficulty of localized disease detection, our method outperforms a global classifier. As our data shows (See Fig. 3), global classification can be unreliable even when the label is correct as the classifier might find the correct label for the wrong reason at an irrelevant spot.

Acknowledgements. This work was supported by the [Rensselaer-IBM AI Research Collaboration](#), part of the [IBM AI Horizons Network](#).

References

1. Cai, J., Lu, L., Harrison, A.P., Shi, X., Chen, P., Yang, L.: Iterative attention mining for weakly supervised thoracic disease pattern localization in chest X-rays. In: Frangi, A.F., Schnabel, J.A., Davatzikos, C., Alberola-López, C., Fichtinger, G. (eds.) MICCAI 2018. LNCS, vol. 11071, pp. 589–598. Springer, Cham (2018). https://doi.org/10.1007/978-3-030-00934-2_66
2. Chen, B., Li, J., Lu, G., Yu, H., Zhang, D.: Label co-occurrence learning with graph convolutional networks for multi-label chest x-ray image classification. *IEEE J. Biomed. Health Inform.* **24**(8), 2292–2302 (2020)
3. Chen, B., Zhang, Z., Lin, J., Chen, Y., Lu, G.: Two-stream collaborative network for multi-label chest x-ray image classification with lung segmentation. *Pattern Recogn. Lett.* **135**, 221–227 (2020)
4. Filice, R.W., et al.: Crowdsourcing pneumothorax annotations using machine learning annotations on the NIH chest X-ray dataset. *J. Digit. Imaging* **33**(2), 490–496 (2020)
5. Gabruseva, T., Poplavskiy, D., Kalinin, A.: Deep learning for automatic pneumonia detection. In: Proceedings of the IEEE/CVF Conference on Computer Vision and Pattern Recognition Workshops, pp. 350–351 (2020)
6. Gordienko, Y., et al.: Deep learning with lung segmentation and bone shadow exclusion techniques for chest X-ray analysis of lung cancer. In: Hu, Z., Petoukhov, S., Dychka, I., He, M. (eds.) ICCSEEA 2018. AISC, vol. 754, pp. 638–647. Springer, Cham (2019). https://doi.org/10.1007/978-3-319-91008-6_63
7. Grover, A., Leskovec, J.: node2vec: scalable feature learning for networks. In: Proceedings of the 22nd ACM SIGKDD International Conference on Knowledge Discovery and Data Mining, pp. 855–864 (2016)
8. He, K., Zhang, X., Ren, S., Sun, J.: Deep residual learning for image recognition. In: Proceedings of the IEEE Conference on Computer Vision and Pattern Recognition, pp. 770–778 (2016)
9. Honnibal, M., Montani, I., Van Landeghem, S., Boyd, A.: spaCy: Industrial-strength Natural Language Processing in Python. Zenodo (2020)
10. Huang, G., Liu, Z., Van Der Maaten, L., Weinberger, K.Q.: Densely connected convolutional networks. In: Proceedings of the IEEE Conference on Computer Vision and Pattern Recognition, pp. 4700–4708 (2017)
11. Irvin, J., et al.: CheXpert: a large chest radiograph dataset with uncertainty labels and expert comparison. In: Proceedings of the AAAI Conference on Artificial Intelligence, vol. 33, pp. 590–597 (2019)
12. Johnson, A.E., et al.: MIMIC-CXR, a de-identified publicly available database of chest radiographs with free-text reports. *Sci. Data* **6**, 1–8 (2019)
13. Kipf, T.N., Welling, M.: Semi-supervised classification with graph convolutional networks. In: International Conference on Learning Representations (2017)
14. Li, C.Y., Liang, X., Hu, Z., Xing, E.P.: Hybrid retrieval-generation reinforced agent for medical image report generation. [arXiv:1805.08298](https://arxiv.org/abs/1805.08298) (2018)
15. Li, Y., Tarlow, D., Brockschmidt, M., Zemel, R.: Gated graph sequence neural networks. In: International Conference on Learning Representations (2016)
16. Liu, D., Xu, S., Zhou, P., He, K., Wei, W., Xu, Z.: Dynamic graph correlation learning for disease diagnosis with incomplete labels. [arXiv:2002.11629](https://arxiv.org/abs/2002.11629) (2020)
17. Mao, C., Yao, L., Luo, Y.: ImageGCN: multi-relational image graph convolutional networks for disease identification with chest X-rays. [arXiv:1904.00325](https://arxiv.org/abs/1904.00325) (2019)

18. Rajpurkar, P., et al.: CheXNet: radiologist-level pneumonia detection on chest X-rays with deep learning. [arXiv:1711.05225](#) (2017)
19. Ren, S., He, K., Girshick, R., Sun, J.: Faster R-CNN: towards real-time object detection with region proposal networks. [arXiv:1506.01497](#) (2015)
20. Selvaraju, R.R., Cogswell, M., Das, A., Vedantam, R., Parikh, D., Batra, D.: Grad-CAM: visual explanations from deep networks via gradient-based localization. In: Proceedings of the IEEE International Conference on Computer Vision (2017)
21. Shih, G., et al.: Augmenting the national institutes of health chest radiograph dataset with expert annotations of possible pneumonia. *Radiol. Artif. Intell.* (2019)
22. Sirazitdinov, I., Kholiavchenko, M., Mustafaev, T., Yixuan, Y., Kuleev, R., Ibragimov, B.: Deep neural network ensemble for pneumonia localization from a large-scale chest X-ray database. *Comput. Electr. Eng.* **78**, 388–399 (2019)
23. Tang, J., Qu, M., Wang, M., Zhang, M., Yan, J., Mei, Q.: LINE: large-scale information network embedding. In: Proceedings of the 24th International Conference on World Wide Web, pp. 1067–1077 (2015)
24. Veličković, P., Cucurull, G., Casanova, A., Romero, A., Lio, P., Bengio, Y.: Graph attention networks. In: International Conference on Learning Representations (2018)
25. Wang, H., et al.: GraphGAN: graph representation learning with generative adversarial nets. In: Proceedings of the AAAI Conference on Artificial Intelligence, vol. 32 (2018)
26. Wang, X., Girshick, R., Gupta, A., He, K.: Non-local neural networks. In: Proceedings of the IEEE Conference on Computer Vision and Pattern Recognition, pp. 7794–7803 (2018)
27. Wang, X., Peng, Y., Lu, L., Lu, Z., Bagheri, M., Summers, R.M.: ChestX-ray8: hospital-scale chest X-ray database and benchmarks on weakly-supervised classification and localization of common thorax diseases. In: Proceedings of the IEEE Conference on Computer Vision and Pattern Recognition, pp. 2097–2106 (2017)
28. Wang, X., Peng, Y., Lu, L., Lu, Z., Summers, R.M.: TieNet: text-image embedding network for common thorax disease classification and reporting in chest X-rays. In: Proceedings of the IEEE Conference on Computer Vision and Pattern Recognition, pp. 9049–9058 (2018)
29. Wu, J., et al.: Automatic bounding box annotation of chest X-ray data for localization of abnormalities. In: 2020 IEEE 17th International Symposium on Biomedical Imaging (ISBI), pp. 799–803. IEEE (2020)
30. Wu, J.T., Syed, A., Ahmad, H., et al.: AI accelerated human-in-the-loop structuring of radiology reports. In: American Medical Informatics Association (AMIA) Annual Symposium (2020)
31. Wu, Z., Pan, S., Chen, F., Long, G., Zhang, C., Philip, S.Y.: A comprehensive survey on graph neural networks. *IEEE Trans. Neural Netw. Learn. Syst.* **32**, 4–24 (2020)
32. You, J., Ying, R., Ren, X., Hamilton, W., Leskovec, J.: GraphRNN: generating realistic graphs with deep auto-regressive models. In: International Conference on Machine Learning, pp. 5708–5717. PMLR (2018)
33. Zeiler, M.D., et al.: On rectified linear units for speech processing. In: 2013 IEEE International Conference on Acoustics, Speech and Signal Processing, pp. 3517–3521. IEEE (2013)
34. Zhou, Y., Zhou, T., Zhou, T., Fu, H., Liu, J., Shao, L.: Contrast-attentive thoracic disease recognition with dual-weighting graph reasoning. *IEEE Trans. Med. Imaging* **40**, 1196–1206 (2021)